10

The crystal structure and optical properties of $Bi_2Mg_{1-x}Cr_xTa_2O_{9+\Delta}$ with a pyrochlore structure

© D.A. Ketova[1], M.G. Krzhizhanovskaya[2], A.A. Selyutin[2], N.A. Zhuk[1]

[1] Syktyvkar State University, Syktyvkar, Russia
[2] St. Petersburg State University, St. Petersburg, Russia

e-mail: deika.160904@gmail.com

Received May 03, 2025
Revised June 09, 2025
Accepted October 24, 2025

The crystal structure and optical properties of solid solutions $Bi_2Mg_{1-x}Cr_xTa_2O_{9+\Delta}$ ($x \leq 0.7$) with a disordered pyrochlore structure (space group $Fd\bar{3}m$: setting 2). With increasing magnesium content, the lattice parameter increases from 10.45852(1) Å ($x(Mg) = 0.3$) to 10.49991(1) ($x(Mg) = 0.7$). Chromium-rich samples exhibit green coloration with reflection in the green 552−558 nm and red □710 nm regions. The width of the band gap for direct allowed electronic transitions varies in the range 2.14−2.29 eV depending on the chromium(III) ion content. Chromium doping reduces the photoactivity of bismuth-containing pyrochlore.

Keywords: chromium, magnesium, pyrochlore, structure, optical properties.

DOI: 10.61011/EOS.2025.10.62558.7997-25

Introduction

Synthetic pyrochlores attract intense scientific interest due to their practically useful physicochemical properties, such as proton conductivity, excellent photocatalytic and dielectric properties [1,2]. The flexibility of the pyrochlore crystal structure toward cation substitutions and vacancies in the anion sublattice enables significant variation in the chemical composition of compounds and the creation of compositions with diverse functional properties. Recently, researchers' main efforts have focused on discovering new representatives of this family of compounds, including high-entropy and multi-element pyrochlores, as well as pyrochlores with oxygen-free or mixed-type anion sublattices [3,4]. Oxide pyrochlores $A_2B_2O_7$ consist of interpenetrating cation sublattices B_2O_6 and A_2O' and form through combinations of divalent and pentavalent cations ($A_2^{2+}B_2^{+5}O_7$) or trivalent and tetravalent cations ($A_2^{3+}B_2^{+4}O_7$) in the A and B sublattices [5]. The B_2O_6 cation sublattice is formed by corner-sharing [BO_6] octahedra. The A_2O' sublattice has an anticristobalite structure formed by [$O'A_4$] tetrahedra. Relatively small cations (Ti^{4+}, Ta^{5+}) occupy B-site positions, while large A-site ions A (Pb^{2+}, Bi^{3+}) reside in 8-vertex polyhedra formed by oxygen atoms from the A_2O' and B_2O_6 sublattices [5]. Mixed bismuth-containing pyrochlores are known, in which the crystal framework is formed by trivalent and pentavalent elements and stabilized by introducing divalent or trivalent cations M (M-Mg, 3*d*-elements) comparable in size to the B ion. Such doping variants lead to the formation of a defect structure in the A cation sublattice, as observed in bismuth-containing pyrochlores. Due to the potential influence of the stereochemically active $6s^2$ electron pair of bismuth ions, the bismuth sublattice remains partially vacant. This results in relaxation properties of the ceramics and a spin glass state [6]. Most bismuth tantalate-based pyrochlores exhibit nanoscale microstructure formed during ceramic synthesis and are promising as photocatalysts. Chromium-containing pyrochlores based on bismuth tantalate have been studied insufficiently [7,8]. Scientists' primary focus has been on detailed qualitative investigation of the crystal structure features using the example of the pyrochlore composition $Bi_{2-x}(CrTa)O_{7-y}$, as well as studies of chromium ion charge states and dielectric properties of oxide ceramics. This work determines the geometric structure parameters, microstructure, and optical properties of $Bi_2Mg_{1-x}Cr_xTa_2O_{9+\Delta}$pyrochlore depending on the molar ratio $n(Mg)/n(Cr)$.

Experimental part

Samples of $Bi_2Mg_{1-x}Cr_xTa_2O_{9+\Delta}$ ($x = 0.3, 0.5, 0.7$) were synthesized by standard ceramic technology from oxides MgO, Bi_2O_3, Cr_2O_3, Ta_2O_5 [8]. Microstructure and local elemental composition of the samples were investigated using scanning electron microscopy and energy-dispersive X-ray spectroscopy (Tescan VEGA 3LMN electron scanning microscope, INCA Energy 450 energy-dispersive spectrometer). The crystal structure was studied by powder X-ray diffraction using a Rigaku Ultima IV diffractometer ($Co_{K\alpha}$air atmosphere, 40 kV/30 mA, Bragg-Brentano geometry) equipped with a position-sensitive detector featuring plastic scintillator strips D/teX Ultra. The 2θ angle was verified before each measurement at room temperature using silicon as an external standard; the zero-shift variation did not exceed $\pm 0.02^\circ$ 2θ. The crystal structure of chromium- and magnesium-doped bismuth tantalate was refined at 25 °C by the Rietveld method using

the Topas 5.0 software package [9]. The Thompson-Cox-Hastings pseudo-Voigt function was used to describe the reflection profiles. Neutral atom scattering factors were applied for all atoms. Site occupancies were determined according to the stoichiometry of the composition. Diffuse reflection spectra were recorded in the 200–900 nm range using a Shimadzu UV-2550 spectrophotometer with a spectral step of 1 nm. Halogen and deuterium lamps served as radiation sources. Spectra were obtained for substances in a barium sulfate matrix. The reflection spectrum of the pure barium sulfate matrix was subtracted from the resulting spectrum. For quantitative description of the diffuse reflection spectra, the Kubelka-Munk theory was applied. The forbidden band width was determined from the position of the fundamental absorption edge according to the Tauc equation:

$$\left(h\nu F(r)\right)^{1/n} = A(h\nu - E_g),$$

where E_g is the band gap width, h is Planck's constant, ν is the frequency of electromagnetic wave oscillations, and $F(r) = (1-r)^2/2r$ s the Kubelka-Munk function. The exponent value for direct allowed transitions equals $n = 1/2$. Diffuse reflection spectra were plotted in Tauc coordinates: $\left(h\nu F(r)\right)^2 = f(E,\ \text{eV})$.

Results and Discussion

X-ray phase analysis data indicate that $Bi_2Mg_{1-x}Cr_xTa_2O_{9+\Delta}$ $(x = 0.3, 0.5, 0.7)$ samples are single-phase (Fig. 1). Analysis of reflection broadenings confirmed cubic crystal structure symmetry ($Fd\bar{3}m$, PDF 00-060-0282) corresponding to the pyrochlore structure. With increasing magnesium content in the samples, the lattice parameter increases uniformly from 10.45852(1) Å $(x(\text{Mg}) = 0.3)$ to 10.49991(1) $(x(\text{Mg}) = 0.7)$. The ionic radius of magnesium(II) cations exceeds that of octahedrally coordinated tantalum(V) cations(V) $(R(\text{Mg}^{2+})_{\text{cn6}} = 0.72\,\text{Å},\ R(\text{Ta}^{5+})_{\text{cn6}} = 0.64\,\text{Å})$, but is smaller than that of 8-coordinated bismuth(III) ions $(R(\text{Bi}^{3+})_{\text{cn8}} = 1.17\,\text{Å}, R(\text{Mg}^{2+})_{\text{cn8}} = 0.89\,\text{Å})$ [10].

This lattice constant increase results from the distribution of larger magnesium(II) ions into octahedral positions of tantalum(V) and chromium(III), whose ionic radii are smaller than that of magnesium(II) $(R(\text{Mg}^{2+})_{\text{cn6}} = 0.72\,\text{Å}, R(\text{Cr}^{3+})_{\text{cn6}} = 0.615\,\text{Å})$. The oxidation state of chromium(III) ions in the pyrochlore composition was determined by NEXAFS spectroscopy in [8]. The calculated unit cell parameters of the solid solutions are comparable to values reported in [7,8] for chromium-containing pyrochlores $Bi_{2-x}(CrTa)O_{7-y}$ $(a = 10.451\,\text{Å})$, $Bi_{1.6}Cr_{0.8}Ta_{1.6}O_{7.6}$ $(a = 10.455\,\text{Å})$ and$_2CrNb_2O_{9+y}$ $(a = 10.459\,\text{Å})$, considering that the ionic radii of Ta(V) and Nb(V) are equal $((R(\text{Nb(V)/Ta(V)})_{\text{cn6}} = 0.064\,\text{nm})$. Powder X-ray diffraction data refined by the Rietveld method provided structural refinement for compositions $Bi_2Mg_{1-x}Cr_xTa_2O_{9+\Delta}$ $(x = 0.3$ and $0.7)$. The best agreement between experimental and calculated diffractograms was achieved for the disordered structure model (space group $Fd\bar{3}m$: setting 2), in which the high-symmetry crystallographic positions of bismuth(III) ions $16d$ are split into 6 equivalent positions $96g$ with 1/6 occupancy of the original [5]. Tantalum(V), magnesium(II), and chromium(III) ions occupy a single set of crystallographic positions $(16b)$ in a 67:33 ratio, respectively. Oxygen ions are disordered and occupy two crystallographic positions, one of which $(48f)$ is fully occupied, while the other $(8a)$ is deficient, filled to 60 % $(x(\text{Cr}) = 0.7)$ and 57 % $(x(\text{Cr}) = 0.3)$ due to heterovalent substitution of octahedral positions by low-charge magnesium(II) and chromium(III) ions.

The stoichiometric formulas of the nominal compositions $Bi_2Mg_{1-x}Cr_xTa_2O_{9+\Delta}$ for $x = 0.7$ and 0.3 (or normalized compositions to 7 oxygen atoms — $Bi_{1.4}Mg_{0.21}Cr_{0.49}Ta_{1.4}O_{6.54}$ and $Bi_{1.4}Mg_{0.49}Cr_{0.21}Ta_{1.4}O_{6.40}$) determined from structure refinement, correspond to compositions with a deficient bismuth cation sublattice — $Bi_{1.41}Cr_{0.44}Mg_{0.22}Ta_{1.33}O_{6.60}$ and $Bi_{1.44}Cr_{0.22}Mg_{0.44}Ta_{1.33}O_{6.57}$ respectively (Table 1). Experimental, calculated, and difference diffractograms for $Bi_2Mg_{1-x}Cr_xTa_2O_{9+\Delta}$ $(x = 0.7$ and $0.3)$ are shown in Fig. 1; atomic and geometric parameters are presented in Table 2. According to the modeling results, tantalum, magnesium, and chromium atoms form a slightly distorted TaO_6 octahedron with Ta-O bond lengths not exceeding 1.99 Å, which is smaller compared to analogous Fe,Mg-doped pyrochlores (1.9959 Å, $x = 0.5$) [11]. This can be explained by the smaller ionic radius of Cr(III) compared to Fe(III) ions $(R(\text{Fe}^{3+})_{\text{cn6}} = 0.645\,\text{Å}$, $R(\text{Cr}^{3+})_{\text{cn6}} = 0.615\,\text{Å})$. Notably, as chromium content decreases, the bond lengths in the octahedron increase, which is fully consistent with the trend in lattice parameters of the solid solutions. Individual interatomic distances in the weakly ordered BiO_8 polyhedron vary from 2.29 to 2.99 Å(Table 2), while the size of the bismuth polyhedron slightly increases with rising magnesium content in the samples.

The asymmetry of the bismuth polyhedron is due to the influence of the stereochemically active $6s^2$ electron pair of bismuth ions. The sample microstructure is porous and dendrite-like, formed by weakly aggregated elongated particles (Fig. 2). Microphotographs reveal local grain coalescence forming larger aggregates. No reliable dependence of crystallite size on the magnesium/chromium ratio was established. The average crystallite size determined by the Scherrer method for the solid solutions is ~ 63 nm while larger grains with longitudinal dimensions of $\sim 0.5\,\mu$m were observed by scanning electron microscopy.

Local quantitative analysis by EDS confirmed that the experimental sample compositions match the nominal ones, while elemental mapping demonstrated uniform Cr/Mg atom distribution across sample surfaces. Diffuse reflection spectra of $Bi_2Mg_{1-x}Cr_xTa_2O_{9+\Delta}$ $(x \le 0.7)$ solid solution samples are shown in Fig. 3.

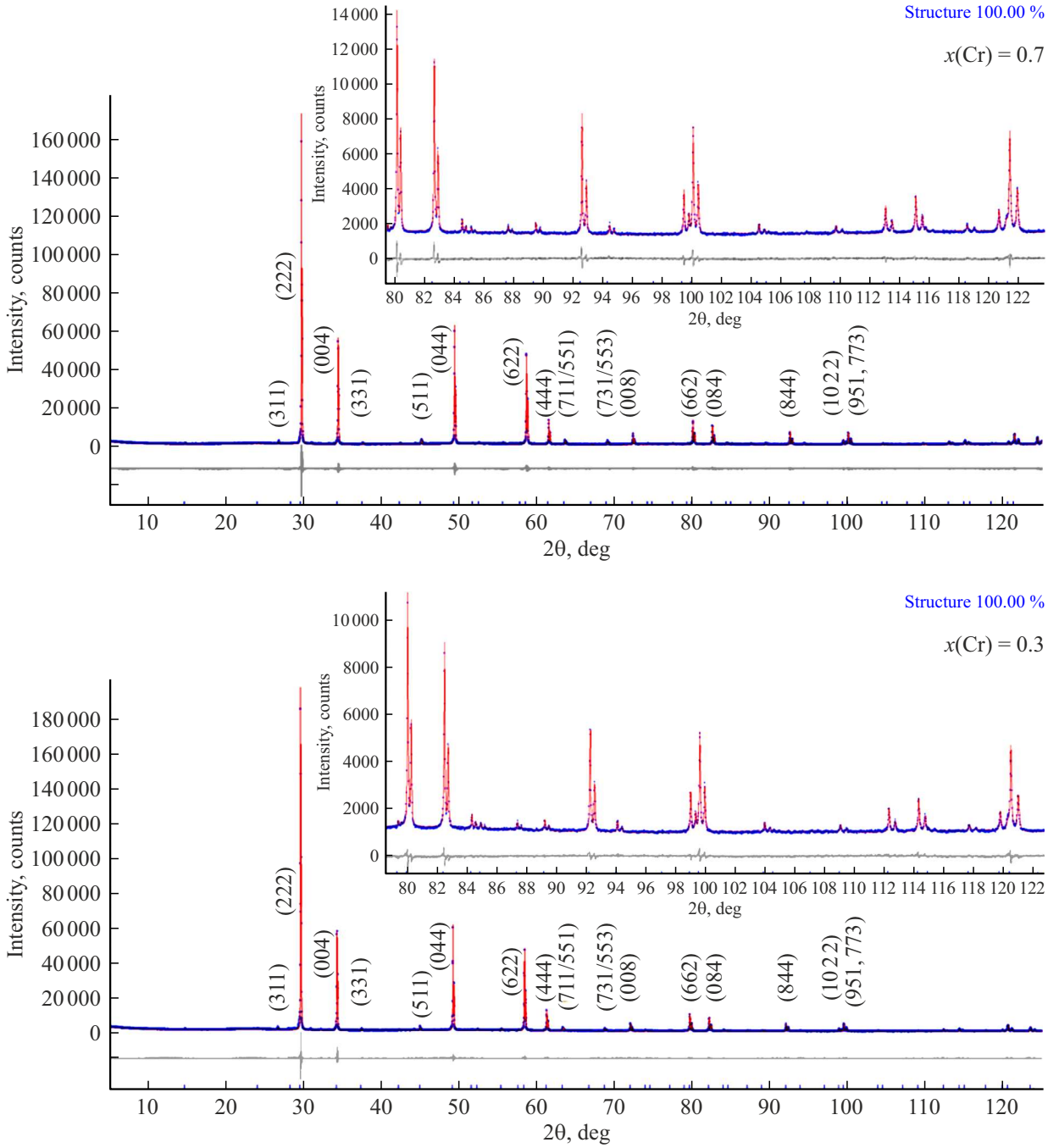

Figure 1. Experimental (blue line), calculated (red line), and difference (gray line) X-ray diffraction patterns of $Bi_2Mg_{1-x}Cr_xTa_2O_{9+\Delta}$ ($x = 0.3$ and 0.7).

The band gap width (E_g) of chromium-containing pyrochlores for direct allowed electronic transitions was estimated from diffuse reflectance spectra (Fig. 3) for samples with different chromium contents $x = 0.3, 0.5$ and 0.7. As Fig. 3 shows, the samples exhibit significant reflection in the green region (552–558 nm). Reflection in the green visible range corresponds to the emerald-green coloration of the samples. A weak reflex is observed in the red region (□710 nm). We suggest that reflection at 710 nm may be associated with a small amount of Cr(VI) ions. From an electronic balance perspective, the system benefits from Cr(VI) ions over Cr(III), as this reduces structural strain in the pyrochlore caused by oxygen vacancies due to heterovalent substitution of Ta(V) ions by chromium. Chromium pyrochlore absorption spectra feature several characteristic bands. Absorption below 400 nm may be due to interband transitions. As shown in [12,13], the shoulder at 450–520 nm is associated with the $d-d$ electronic transition

Table 1. Atomic parameters in $Bi_2Mg_{1-x}Cr_xTa_2O_{9+\Delta}$ for $x = 0.7$ and 0.3

Atom	crystallographic positions	x	y	z	Coefficient popularities	B_{iso}, Å^2
			$x(\mathrm{Cr}) = 0.7$			
Bi	96g	0	−0.02425(12)	0.02425(12)	0.1177(6)	1.70(7)
Ta	16b	0.5000	0.5000	0.5000	0.667	0.73(2)
Cr	16b	0.5000	0.5000	0.5000	0.22	0.73(2)
Mg	16b	0.5000	0.5000	0.5000	0.11	0.73(2)
O1	48f	0.1250	0.1250	0.4320(4)	1.00	1.69(15)
O2	8a	0.1250	0.1250	0.1250	0.60(3)	1.69(15)
			$x(\mathrm{Cr}) = 0.3$			
Bi	96g	0	−0.02471(15)	0.02471(15)	0.1197(7)	2.23(10)
Ta	16b	0.5000	0.5000	0.5000	0.667	1.18(3)
Cr	16b	0.5000	0.5000	0.5000	0.11	1.18(3)
Mg	16b	0.5000	0.5000	0.5000	0.22	1.18(3)
O1	48f	0.1250	0.1250	0.4323(5)	1.00	2.39(19)
O2	8a	0.1250	0.1250	0.1250	0.57(4)	2.39(19)

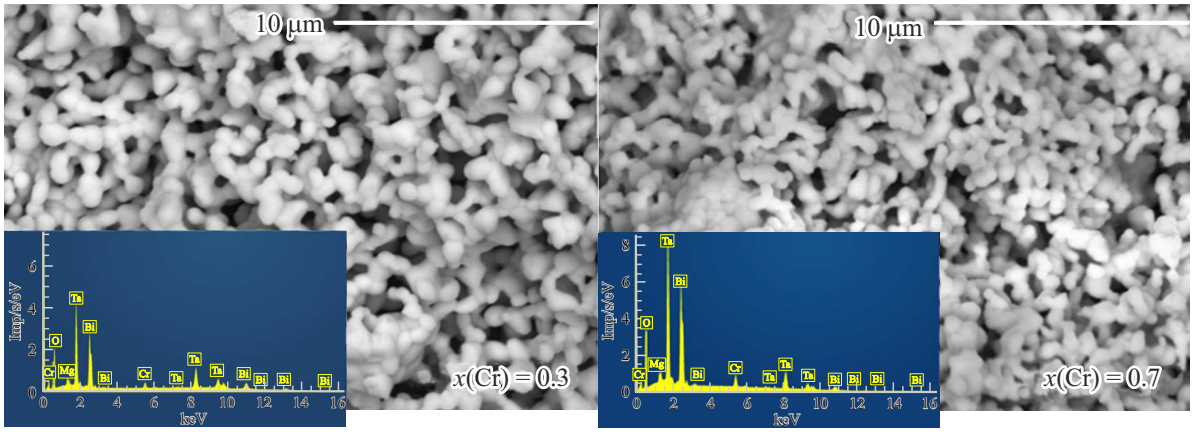

Figure 2. Microphotographs and EDS of $Bi_2Mg_{1-x}Cr_xTa_2O_{9+\Delta}$ samples ($x = 0.7$ and 0.3) in secondary electron mode.

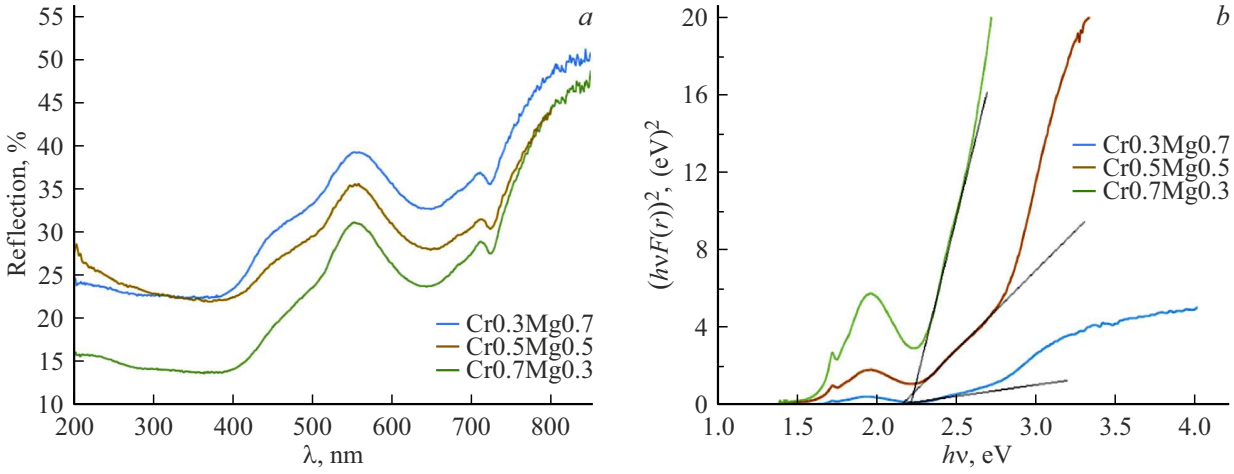

Figure 3. Diffuse reflection spectra (a) and Tauc plots (b) for $Bi_2Mg_{1-x}Cr_xTa_2O_{9+\Delta}$ samples.

Table 2. Structural parameters and agreement factors obtained for solid solutions $Bi_2Mg_{1-x}Cr_xTa_2O_{9+\Delta}$ ($x = 0.7$ and 0.3) from Rietveld refinement

Index x(Cr)	0.7	0.3
a (Å)	10.45852(3)	10.49991(5)
α, β, γ (°)	90, 90, 90	90, 90, 90
V (Å^3)	1143.959(11)	1157.595(18)
D_{calc} (q/cm^3)	7.785(18)	7.68(2)
R_B (%)	0.60	0.68
R_{wp} (%)	4.10	4.73
R_p (%)	3.05	3.49
R_{exp} (%)	2.19	2.29
GOF	1.87	2.07
	Bond lengths (Å)	
Bi1−O1×2	2.293(2)	2.3027(3)
−O1×2	2.354(4)	2.360(4)
−O1×2	2.678(3)	2.692(4)
−O2×2	2.966(4)	2.987(4)
⟨Bi1$_{VIII}$−O⟩	2.57	2.58
Ta1−O1×6	1.9808(16)	1.9874
⟨Ta1$_{VI}$−O⟩	1.98	1.99

$4A_2 \rightarrow 4T_1$ characteristic of Cr(III) ions. Broad absorption at 600−700 nm with a maximum at 650 nm corresponds to the $4A_2 \rightarrow 4T_2$ transition and is also observed in Cr(III) salt solutions, indicating chromium(III) ions in octahedral positions. Calculations show that the band gap width for direct allowed transitions in samples $x(\mathrm{Cr}) = 0.3$, 0.5 and 0.7 is 2.14, 2.22, and 2.29 eV (Fig. 3), corresponding to absorption in the 545−583 nm wavelength range. With increasing chromium content, the band gap width increases, and the energy gap between the valence and conduction bands grows. Thus, chromium doping reduces the photoactivity of bismuth-containing pyrochlore. Nevertheless, the forbidden band width of the studied ceramics is close to the energy of solar radiation reaching Earth's surface at maximum intensity (2.1−2.5 eV). making these materials promising for use as light-absorbing elements in solar cells.

Conclusions

This work examines the crystal structure features and optical properties of $Bi_2Mg_{1-x}Cr_xTa_2O_{9+\Delta}$ solid solutions. The samples exhibit significant reflection in the green region. With increasing chromium content, the forbidden band width increases from 2.14 ($x(\mathrm{Cr}) = 0.3$) to 2.29 eV ($x(\mathrm{Cr}) = 0.7$) and the energy gap between the valence and conduction bands grows.

Acknowledgment

The structure investigation was conducted at the Resource Center for Diffraction Methods of Research, Scientific Park of St. Petersburg State University, under project 125021702335-5. Diffuse reflection spectra were obtained using equipment from the Resource Center of the Scientific Park of St. Petersburg State University „Methods of Substance Composition Analysis".

Conflict of interest

The authors declare that they have no conflict of interest.

References

[1] S. Murugesan, M.N. Huda, Y. Yan, M.M. Al-Jassim, V. (Ravi) Subramanian. J. Phys. Chem. C, **114**, 10598–10605 (2010). DOI: 10.1021/jp906252r
[2] G. Giampaoli, T. Siritanon, B. Day, J. Li, M.A. Subramanian. Prog. Solid State Chem., **50**, 16–23 (2018). DOI: 10.1016/j.progsolidstchem.2018.06.001
[3] Z. Teng, L. Zhu, Y. Tan, S. Zeng, Y. Xia, Y. Wang, H. Zhang. J. Eur. Ceram. Soc., **40**, 1639–1643 (2020). DOI: 10.1016/j.jeurceramsoc.2019.12.008
[4] D. Reig-i-Plessis, A.M. Hallas. Phys. Rev. Materials, **5**, 030301 (2021). DOI: 10.1103/PhysRevMaterials.5.030301
[5] M.A. Subramanian, G. Aravamudan, G.V. Subba Rao. Prog. Solid State Chem., **15**, 55–143 (1983). DOI: 10.1016/0079-6786(83)90001-8
[6] J.E. Greedan. J. Alloys. Comp., **408−412**, 444–455 (2006). DOI: 10.1016/j.jallcom.2004.12.084
[7] T. Kamiyama, K. Oikawa, A. Hoshikawa, B.J. Kennedy, Y. Kubota, K. Kato. Mater. Res. Bull., **39**, 553–560 (2004). DOI: 10.1016/j.materresbull.2003.12.017
[8] N.A. Zhuk, N.A. Sekushin, M.G. Krzhizhanovskaya, A.V. Koroleva, A.A. Reveguk, S.V. Nekipelov, D.V. Sivkov, V.P. Lutoev, B.A. Makeev, V.V. Kharton, A.M. Lebedev, R.G. Chumakov, K.D. Koksharova, A.D. Shpynova. Mater. Res. Bull., **158**, 112067 (2023). DOI: 10.1016/j.materresbull.2022.112067
[9] Topas 5.0. General profile and structure analysis software for powder diffraction data (Bruker AXS, Karlsruhe, 2014).
[10] R.D. Shannon. Acta Crystallogr. A, **32**, 751–767 (1976). DOI: 10.1107/s0567739476001551
[11] N.A. Zhuk, M.G. Krzhizhanovskaya, A.V. Koroleva, V.G. Semenov, A.A. Selyutin, A.M. Lebedev, S.V. Nekipelov, D.V. Sivkov, V.V. Kharton, V.P. Lutoev et al. Inorganics, **11** (1), 8 (2023). DOI: 10.3390/inorganics11010008
[12] N. Serpone, D. Lawless, J. Disdier, J.-M. Herrmann. Langmuir, **10**, 643–652 (1994). DOI: 10.1021/LA00015A010
[13] R.S. Pavlov, V.B. Marza, J.B. Carda. J. Mater. Chem., **12**, 2825–2832 (2002). DOI: 10.1039/b201802k

Translated by J.Savelyeva